J. Appl. Comput. Mech., 7(4) (2021) 2049–2063
DOI: 10.22055/JACM.2020.32423.2027

ISSN: 2383-4536
jacm.scu.ac.ir

Shahid Chamran University of Ahvaz

Journal of Applied and Computational Mechanics

Research Paper

Improvement of Numerical Manifold Method using Nine-node Quadrilateral and Ten-node Triangular Elements along with Complex Fourier RBFs in Modeling Free and Forced Vibrations

Mohammad Malekzadeh[1], Saleh Hamzehei-Javaran[2], Saeed Shojaee[3]

[1] Civil Engineering Department, Shahid Bahonar University of Kerman, Pajoohesh Square, Kerman, P. O. Box 76169-133, Iran, Email: malekzadeh7@gmail.com
[2] Civil Engineering Department, Shahid Bahonar University of Kerman, Pajoohesh Square, Kerman, P. O. Box 76169-133, Iran, Email: s.hamzeheijavaran@uk.ac.ir
[3] Civil Engineering Department, Shahid Bahonar University of Kerman, Pajoohesh Square, Kerman, P. O. Box 76169-133, Iran, Email: saeed.shojaee@uk.ac.ir

Received February 02 2020; Revised April 10 2020; Accepted for publication April 17 2020.
Corresponding author: S. Hamzehei-Javaran (s.amzeheijavaran@uk.ac.ir)

Abstract. In this paper, the numerical manifold method (NMM) with a 9-node quadrilateral element and a 10-node triangular element is developed. Furthermore, complex Fourier shape functions are used to improve the 9-node quadrilateral NMM. Also, the two approaches of higher-order NMM construction are compared, increasing the order of weight functions or local approximation ones; for this purpose, six-node triangular and three-node triangular using second-order and third-order NMM is used. For validation of the suggested method, one free vibration and two forced vibration numerical examples are assessed. The results show that the proposed methods are more accurate than conventional NMM. In addition, the superiority of complex Fourier shape functions compared to classical Lagrange ones in improving accuracy is perceived.

Keywords: Numerical manifold method, Nine-node complex Fourier shape functions, Complex Fourier radial basis functions, Free vibrations, Forced vibrations, Ten-node shape functions.

1. Introduction

The numerical manifold method (NMM), which combines the finite element method (FEM) and the discontinuous deformation analysis (DDA), was proposed by Shi in 1992 [1,2]. The use of two separate covers, mathematical covers, and physical ones give this method the ability to analyze continuous and discontinuous problems in a unified way [3]. Mathematical covers consist of mathematical functions, and physical covers define geometry, constraints, etc.

Many researchers tried to improve NMM; For instance, the governing equations of NMM usually derive from the minimum potential energy principle (MPE), but Li et al. [4] used the weighted residual method in NMM and achieved results resembling those of MPE. Also, some researchers like Oden et al. [5], Ghasemzadeh et al. [6], and Fan et al. [7] tried to solve the linear dependence problem of NMM. Zheng and Xu [8] proposed new treatment in solving linear elastic fracture problems, Chen and Li [9] try to improved NMM in generating manifold elements and Chern et al. [10] developed a second-order displacement function for NMM.

Usually, the use of 3-node triangular elements, because of simplicity in use and better adaptation on the physical domain, is common in NMM (also in FEM [11-14]). Shyu and Salami [15] proposed a manifold method with Four-node isoparametric element, Zhang et al. [16] used 6-node triangular elements and Fan et al. [17] used 9-node triangular elements to improve NMM's accuracy and observed that the extended NMM could also solve simulate large deformation and contact problems in continuous and discontinuous problems. In this paper, in addition to the 3-node and 6-node triangular element, 10-node triangular and 9-node quadrilateral element are used. Although, functions of the mentioned covers can be chosen arbitrary according to the physical features; usually these functions are chosen from polynomials. In this paper, in addition to choosing weight functions from the polynomials, weight functions are also chosen in a new way by using Fourier functions. The aim of this study is to use the new 9-node quadrilateral element NMM which is produced with new weight functions that are chosen by using Fourier functions and the new 10-node triangular element NMM, and compare the proposed methods with the 6-node and 3-node triangular and also 9-node quadrilateral NMM by the use of polynomials.

The complex Fourier radial basis function (RBF) was introduced by Hamzehei-Javaran et al. [18]. Simultaneous satisfaction of polynomial, exponential and trigonometric function fields is one of the advantages of the suggested shape functions, unlike the classic Lagrange functions that only satisfy polynomial function fields. Some applications of different kinds of RBFs in solving various types of problems are reported in the literature [19-32].

In the following sections include a summary of NMM and the new proposed elements; and also complex Fourier shape functions and their properties and advantages are introduced. Three numerical examples are provided to examine the accuracy

Published online: July 20 2020

and the validity of the 9-node quadrilateral NMM with the new proposed shape functions. The results show that the proposed NMM with the use of complex Fourier shape functions is more accurate than the 3-node triangular and the 9-node quadrilateral NMM with Lagrange shape functions.

2. Brief Introduction of Numerical Manifold Method

The mathematical cover is one of the fundamental concepts of NMM. At first, the whole problem domain must cover with mathematical covers. Mathematical covers are chosen arbitrary, but their assembly must completely cover all physical domain, and they can overlap with each other [33]. By intersecting mathematical covers and physical domain, physical covers are formed. Indeed, physical covers can also be understood as the subdivision of mathematical covers by physical domain. Finally, manifold elements are obtained by overlapping physical covers with each other. Along with the above process, weight functions are constructed over each mathematical cover, and cover functions are chosen for each physical cover. So, NMM combines two kinds of functions together on each manifold element.

Supposing that an element E is formed by m overlapped covers, the global function $u(x,y)$ can be obtained through the weighted average of the local approximations $u_i(x,y)$ using the Partition of Unity (PU) function $w_i(x,y)$ as presented in eq. (1):

$$u(x,y) = \sum_{i=1}^{m} w_i(x,y)\, u_i(x,y) \tag{1}$$

where $w_i(x,y)$, cover weighting function, is defined as one function over the mathematical covers and meets the following conditions depicted in eq. (2) [6]:

$$\begin{cases} 0 \le w_i \le 1, & \forall (x,y) \in M_i \\ w_i = 0, & \forall (x,y) \notin M_i \\ \sum_{i=1}^{m} w_i = 1, & \forall (x,y) \in \Omega \end{cases} \tag{2}$$

where Ω is the whole field.

2.1 Cover weighting functions

It is worth mentioning that a manifold element can span discontinuity boundaries, and can be partially out of the material volume. So, the same shape and size for all the elements are always available, no matter how complicated the geometric shapes of material volumes and joint distributions are. As mentioned above, in this paper in addition to 3-node and 6-node NMM (see [1], [16]), 9-node quadrilateral and 10-node triangular elements are used.

2.1.1 9-node quadrilateral element

A 9-node quadrilateral element consist of overlapping of 9 quadrilateral mathematical covers, which is shown in Fig. 1. Since the development of element matrices and equations expressed in terms of a global coordinate system becomes an enormously task (if even possible), the isoparametric formulation is used for quadrilateral elements [34]. Suppose a manifold element like Fig. 2, the corresponding nine weighting functions in the natural coordinate system can be written as eq. (3).

$$w_l(\xi,\eta) = a_l + b_l\xi + c_l\eta + d_l\xi^2 + e_l\xi\eta + f_l\eta^2 + g_l\xi^2\eta + h_l\xi\eta^2 + i_l\xi^2\eta^2, \quad l = 1,2,3,\ldots,9 \tag{3}$$

Each of the nine cover points of the element should meet the following conditions depicted in eq. (4).

$$w_l(\xi_m,\eta_m) = \delta_{lm}, \quad l,m = 1,2,3,\ldots,9 \tag{4}$$

where

$$\delta_{lm} = \begin{cases} 1 & \text{for} \quad l = m \\ 0 & \text{for} \quad l \ne m \end{cases} \tag{5}$$

Substituting eq. (3) into eq. (4), unknowns ($a_l, b_l, c_l, \ldots, i_l$) can be solved. Equation (6) shows the element weight functions [35]:

$$\begin{cases} \text{corner nodes}: & N_i = \dfrac{1}{4}(1+\xi_0)(1+\eta_0)(\xi_0+\eta_0-1) \\ \text{mid-side nodes}: & \begin{cases} \xi_i = 0 & N_i = \dfrac{1}{2}(1-\xi^2)(1+\eta_0) \\ \eta_i = 0 & N_i = \dfrac{1}{2}(1+\xi_0)(1-\eta^2) \end{cases} \end{cases} \tag{6}$$

where $\xi_0 = \xi\xi_i$, $\eta_0 = \eta\eta_i$ and ξ_i, η_i are the normalized coordinates at node i.

2.1.2 10-node triangular element

Each 10-node triangular element is constructed from the overlap of ten mathematical covers, and as Fig.3 shows each node is the center of a hexagon mathematical cover (Fig. 4 shows an irregular 10-node triangular element). The weight functions for the considered element is as eq. (7).

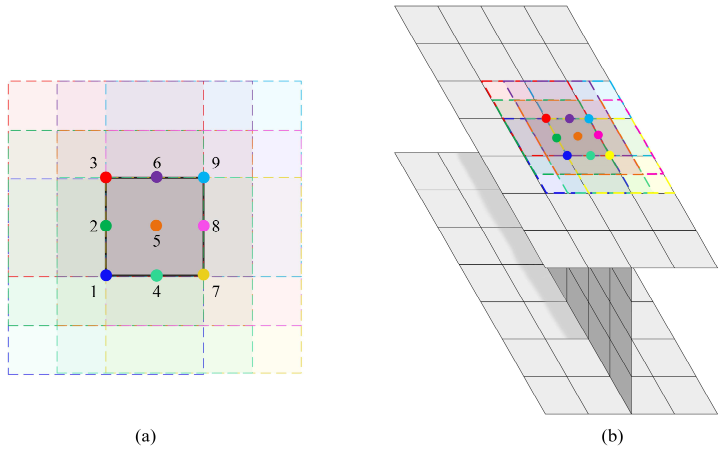

Fig. 1. (a) 9-node quadrilateral manifold element which consist of overlapping of 9 mathematical covers; (b) An IPE which is meshed with 9-node quadrilateral manifold element.

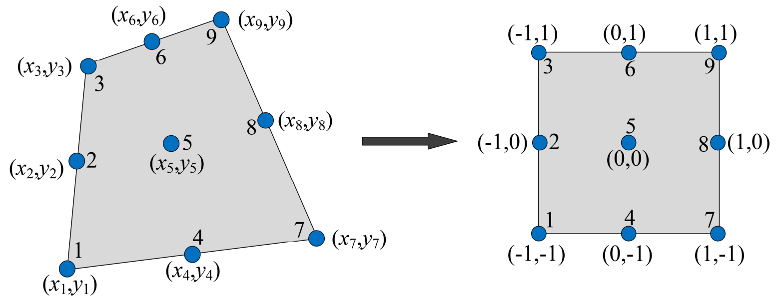

Fig. 2. 9-node quadrilateral element in global and natural coordinate system.

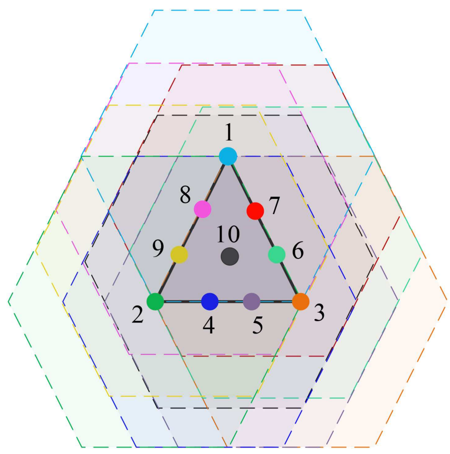

Fig. 3. 10-node triangular manifold element is constructed from overlap of 10 hexagon mathematical covers.

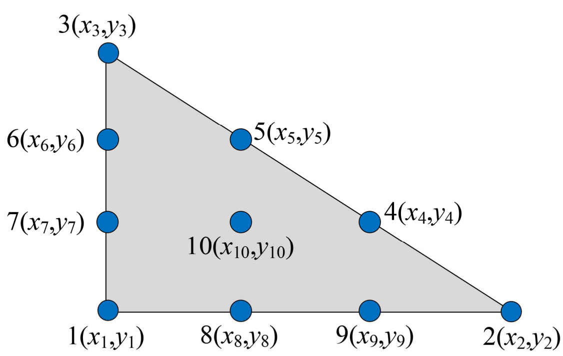

Fig. 4. 10-node triangular element.

$$\begin{aligned} w_1(x,y) &= a_1 + b_1x_1 + c_1y_1 + d_1x_1^2 + e_1x_1y_1 + f_1y_1^2 + g_1x_1^3 + h_1x_1^2y_1 + i_1x_1y_1^2 + j_1y_1^3 \\ w_2(x,y) &= a_2 + b_2x_2 + c_2y_2 + d_2x_2^2 + e_2x_2y_2 + f_2y_2^2 + g_2x_2^3 + h_2x_2^2y_2 + i_2x_2y_2^2 + j_2y_2^3 \\ &\vdots \\ w_{10}(x,y) &= a_{10} + b_{10}x_{10} + c_{10}y_{10} + d_{10}x_{10}^2 + e_{10}x_{10}y_{10} + f_{10}y_{10}^2 + g_{10}x_{10}^3 + h_{10}x_{10}^2y_{10} + i_{10}x_{10}y_{10}^2 + j_{10}y_{10}^3 \end{aligned} \tag{7}$$

The center of these covers is considered as eq. (8) and should meet the eq. (9) conditions.

$$(x_m, y_m), \quad m = 1,2,3,\ldots,10 \tag{8}$$

$$w_l(\xi,\eta) = \delta_{lm}, \quad l,m = 1,2,3,\ldots,10 \tag{9}$$

in which δ_{lm} is as eq. (5).

Substituting eq. (7) in eq. (9), element weight functions are as eq. (10).

$$w_l(x,y) = \mathbf{W}_l\mathbf{L}(x,y), \qquad l = 1,2,\ldots,10 \tag{10}$$

in which

$$\begin{aligned} \begin{bmatrix} \mathbf{W}_1 \\ \mathbf{W}_2 \\ \vdots \\ \mathbf{W}_{10} \end{bmatrix} &= \begin{bmatrix} f_{11} & f_{12} & \cdots & f_{110} \\ f_{21} & f_{22} & & f_{210} \\ \vdots & & \ddots & \\ f_{101} & f_{102} & & f_{1010} \end{bmatrix} \\ &= \left(\begin{bmatrix} 1 & x_1 & y_1 & x_1^2 & x_1y_1 & y_1^2 & x_1^3 & x_1^2y_1 & x_1y_1^2 & y_1^3 \\ 1 & x_2 & y_2 & x_2^2 & x_2y_2 & y_2^2 & x_2^3 & x_2^2y_2 & x_2y_2^2 & y_2^3 \\ & & \vdots & & & & & & & \\ 1 & x_{10} & y_{10} & x_{10}^2 & x_{10}y_{10} & y_{10}^2 & x_{10}^3 & x_{10}^2y_{10} & x_1y_{10}^2 & y_{10}^3 \end{bmatrix}^{-1} \right)^{T} \\ \mathbf{L}(x,y) &= \begin{bmatrix} 1 & x & y & x^2 & xy & y^2 & x^3 & x^2y & xy^2 & y^3 \end{bmatrix}^{T} \end{aligned} \tag{11}$$

2.2 Cover displacement functions

As mentioned, the cover displacement functions are chosen from polynomials by arbitrary degree. So, by increasing the polynomial degree, the manifold degree increases. As a result, in NMM, it is not necessary to add nodes to the element for increasing the order of the displacement function.

The cover displacement functions can be expressed as eq. (12).

$$\begin{aligned} u_l(x,y) &= u_{l0} + u_{l1}x + u_{l2}y + u_{l3}x^2 + u_{l4}xy + u_{l5}y^2 + \cdots + u_{lr}x^n + \cdots + u_{lm}y^n \\ v_l(x,y) &= v_{l0} + v_{l1}x + v_{l2}y + v_{l3}x^2 + v_{l4}xy + v_{l5}y^2 + \cdots + v_{lr}x^n + \cdots + v_{lm}y^n \end{aligned}, \qquad l = 1,2,3,\cdots,9 \tag{12}$$

Equation (12) can also be expressed as:

$$\begin{aligned} u_l(x,y) &= \mathbf{B}_l(x,y)\mathbf{U}_l \\ v_l(x,y) &= \mathbf{B}_l(x,y)\mathbf{V}_l \end{aligned}, \qquad l = 1,2,3,\cdots,9 \tag{13}$$

where

$$\begin{aligned} &\mathbf{B}_l = [1 \quad x \quad y \quad x^2 \quad xy \quad y^2 \quad \cdots \quad x^n \quad \cdots \quad y^n] \\ &\mathbf{U}_l = \begin{bmatrix} u_{l0} \\ u_{l1} \\ u_{l2} \\ \vdots \\ u_{lm} \end{bmatrix}, \quad \mathbf{V}_l = \begin{bmatrix} v_{l0} \\ v_{l1} \\ v_{l2} \\ \vdots \\ v_{lm} \end{bmatrix}, \qquad l = 1,2,3,\cdots,9 \end{aligned} \tag{14}$$

According to eq. (1), the global displacement functions in a manifold element can be written as eq. (15). So, the global displacement functions can be written as eq. (16); in which $\mathbf{T}_l(x,y)$ and $\mathbf{D}_l$ can be expressed as eq. (17).

$$u(x,y) = w_1(x,y)\,u_1(x,y) + w_2(x,y)\,u_2(x,y) + w_3(x,y)\,u_3(x,y) + \cdots + w_9(x,y)\,u_9(x,y) \tag{15}$$

$$\begin{bmatrix} u(x,y) \\ v(x,y) \end{bmatrix} = \begin{bmatrix} \mathbf{T}_1(x,y) & \mathbf{T}_2(x,y) & \cdots & \mathbf{T}_9(x,y) \end{bmatrix} \begin{bmatrix} \mathbf{D}_1 \\ \mathbf{D}_2 \\ \vdots \\ \mathbf{D}_9 \end{bmatrix} \tag{16}$$

$$
\mathbf{T}_l(x,y)=\begin{bmatrix}\mathbf{F}_l & 0\\ 0 & \mathbf{F}_l\end{bmatrix}=\begin{bmatrix}w_l(x,y)\mathbf{B}_l(x,y) & 0\\ 0 & w_l(x,y)\mathbf{B}_l(x,y)\end{bmatrix}
$$
$$
\mathbf{D}_l=\begin{bmatrix}\mathbf{U}_l\\ \mathbf{V}_l\end{bmatrix},\qquad l=1,2,3,\cdots,9 \tag{17}
$$

2.3 Matrices of equilibrium equations

When the displacement functions are obtained, the total potential energy of the field can be expressed. Afterwards, the equilibrium equations can be derived from minimizing the total potential energy and then the coefficients of each cover displacement function can be obtained by solving the equilibrium equations [1,2].

So, using the total potential energy method or the weighted residuals method, equilibrium equations can be derived as follows:

$$
\mathbf{M}\ddot{\mathbf{u}}+\mathbf{K}\mathbf{u}-\mathbf{F}=\mathbf{0} \tag{18}
$$

where $\ddot{\mathbf{u}}$ and $\mathbf{u}$ are displacement and acceleration, respectively. Also, the stiffness matrix $\mathbf{K}$, the mass matrix $\mathbf{M}$ and the loading matrix $\mathbf{F}$ are defined in eq. (19).

$$
\begin{aligned}
\mathbf{M}&=\int_\Omega \rho\mathbf{T}^{\mathrm{T}}\mathbf{T}d\Omega\\
\mathbf{K}&=\int_\Omega \mathbf{G}^{\mathrm{T}}\mathbf{E}\mathbf{G}d\Omega\\
\mathbf{F}&=\int_\Omega \rho\mathbf{T}^{\mathrm{T}}\mathbf{b}d\Omega+\int_{\Gamma_t}\mathbf{T}^{\mathrm{T}}\mathbf{t}_\Gamma d\Gamma_t
\end{aligned} \tag{19}
$$

in which, $\mathbf{b}$ is the body force per unit mass, Γ_t is the boundary of traction, $\mathbf{t}_\Gamma$ is the traction, and $\mathbf{E}$ is defined as follows:

$$
\mathbf{E}=\frac{E}{1-\nu^2}\begin{bmatrix}1 & \nu & 0\\ \nu & 1 & 0\\ 0 & 0 & \frac{1-\nu}{2}\end{bmatrix} \tag{20}
$$

in which E and ν are Young's modulus and Poisson's ratio respectively. For plane strain, E and ν replaced by $E/(1-\nu^2)$ and $\nu/(1-\nu)$.

To determine $\mathbf{G}_l$, the strains in a 9-node quadrilateral element can be obtained from eq. (21) [1,31].

$$
\begin{bmatrix}\varepsilon_x\\ \varepsilon_y\\ \gamma_{xy}\end{bmatrix}=\begin{bmatrix}\frac{\partial u}{\partial x}\\ \frac{\partial v}{\partial y}\\ \frac{\partial u}{\partial y}+\frac{\partial v}{\partial x}\end{bmatrix}=\begin{bmatrix}\mathbf{G}_1 & \mathbf{G}_2 & \mathbf{G}_3 & \cdots & \mathbf{G}_9\end{bmatrix}\begin{bmatrix}\mathbf{D}_1\\ \mathbf{D}_2\\ \mathbf{D}_3\\ \vdots\\ \mathbf{D}_9\end{bmatrix},\qquad l=1,2,3,\cdots,9 \tag{21}
$$

where $\mathbf{D}_l$, l=1,2,…,9 is as eq. (17) and

$$
\mathbf{G}_l=\begin{bmatrix}\frac{\partial\mathbf{F}_l}{\partial x} & 0\\ 0 & \frac{\partial\mathbf{F}_l}{\partial y}\\ \frac{\partial\mathbf{F}_l}{\partial y} & \frac{\partial\mathbf{F}_l}{\partial x}\end{bmatrix} \tag{22}
$$

in which, $\frac{\partial\mathbf{F}_l}{\partial x}$ and $\frac{\partial\mathbf{F}_l}{\partial y}$ are in the form of eq. (23).

$$
\begin{bmatrix}\frac{\partial\mathbf{F}_l}{\partial x}\\ \frac{\partial\mathbf{F}_l}{\partial y}\end{bmatrix}=\mathbf{J}^{-1}\begin{bmatrix}\frac{\partial\mathbf{F}_l}{\partial\xi}\\ \frac{\partial\mathbf{F}_l}{\partial\eta}\end{bmatrix},\qquad l=1,2,3,\ldots,9 \tag{23}
$$

where $\mathbf{J}$ is the Jacobian matrix and can be written as below equation:

$$
\mathbf{J}=\begin{bmatrix}\frac{\partial x}{\partial\xi} & \frac{\partial y}{\partial\xi}\\ \frac{\partial x}{\partial\eta} & \frac{\partial y}{\partial\eta}\end{bmatrix} \tag{24}
$$

3. Complex Fourier Shape Functions

Complex Fourier shape functions have various properties which make them more accurate and stable than other shape functions such as classic Lagrange in the approximation process. In the following, these shape functions are introduced, and some of their properties are presented.

3.1 The basis for the construction of complex Fourier elements

Any function in the functional space can be obtained as constant coefficients multiplied by a series of basis functions [36]. Choosing a suitable set of functions to be implemented as basis functions is very important. In this paper, complex Fourier functions are chosen to be implemented as basis functions. The implementation of complex Fourier functions as RBF has been already reported in the works of Hamzehei-Javaran and Khaji [18, 36-39]. Here, to achieve the advantages of RBFs in the interpolation of state variables, complex Fourier is implemented in an element-based framework with 9-node elements for the approximation of the state variables of Navier's equation (displacements and tractions) [38]. In the following, the enriching process of complex Fourier RBF in the natural coordinates mapping with 9-node is expressed.

3.2 Enrichment of complex Fourier RBF-1D complex Fourier element

The following steps explain the enrichment process of the desirable RBF for a domain with n arbitrary nodes. Firstly, polynomial terms are added to the functional expansion, which only uses RBF in the approximation:

$$u_h(x) = \sum_{i=1}^{n} R_i(r)a_i + \sum_{j=1}^{m} P_j(x)b_j = \mathbf{R}^T(r)\mathbf{a} + \mathbf{P}^T(x)\mathbf{b} \tag{25}$$

where n is the number of nodes, m denotes the basis polynomial terms, r represents the Euclidean norm among data points and

$$\begin{aligned} &\mathbf{a} = [a_1 \quad a_2 \quad \cdots \quad a_n]^T, \quad \mathbf{b} = [b_1 \quad b_2 \quad \cdots \quad b_m]^T \\ &\mathbf{R}(r) = [R_1(r) \quad R_2(r) \quad \cdots \quad R_n(r)], \\ &\mathbf{P}(x) = [P_1(x) \quad P_2(x) \quad \cdots \quad P_m(x)] \end{aligned} \tag{26}$$

Satisfying eq. (25) on the nodal points leads to below equation:

$$\hat{\mathbf{u}} = \mathbf{R}_Q\mathbf{a} + \mathbf{P}_m\mathbf{b} \tag{27}$$

where $\mathbf{R}_Q$ and $\mathbf{P}_m$ are

$$\begin{aligned} \mathbf{R}_Q &= \begin{bmatrix} R_1(r_1) & \cdots & R_n(r_1) \\ \vdots & \ddots & \vdots \\ R_1(r_n) & \cdots & R_n(r_n) \end{bmatrix}_{n\times n}, \\ \mathbf{P}_m &= \begin{bmatrix} P_1(x_1) & \cdots & P_m(x_1) \\ \vdots & \ddots & \vdots \\ P_1(x_n) & \cdots & P_m(x_n) \end{bmatrix}_{n\times m} \end{aligned} \tag{28}$$

There are n+m unknowns in eq. (27), while there are just n equations. Therefore, considering extra conditions is necessary to overcome this challenge; eq. (29) is the condition [40].

$$\sum_{i=1}^{n} P_j(x_i)a_i = 0, \;\; j = \overline{1,m} \quad \rightarrow \quad \mathbf{P}_m^T\mathbf{a} = 0 \tag{29}$$

As a result, the final set of equations can be achieved as below:

$$\begin{bmatrix} \mathbf{R}_Q & \mathbf{P}_m \\ \mathbf{P}_m^T & \mathbf{0} \end{bmatrix}\begin{bmatrix} \mathbf{a} \\ \mathbf{b} \end{bmatrix} = \begin{bmatrix} \hat{\mathbf{u}} \\ \mathbf{0} \end{bmatrix} \tag{30}$$

Finally, after doing some algebraic manipulations, the eq. (31) is obtained:

$$\mathbf{a} = \mathbf{S}_b\hat{\mathbf{u}}\,, \quad \mathbf{b} = \mathbf{S}_a\hat{\mathbf{u}} \tag{31}$$

in which

$$\mathbf{S}_a = \mathbf{R}_Q^{-1} - \mathbf{R}_Q^{-1}\mathbf{P}_m\mathbf{S}_b\,, \quad \mathbf{S}_b = \left[\mathbf{P}_m^T\mathbf{R}_Q^{-1}\mathbf{P}_m\right]^{-1}\mathbf{P}_m^T\mathbf{R}_Q^{-1} \tag{32}$$

Substituting **a** and **b** into eq. (25), leads to the below equation:

$$u_h(x) = \left[\mathbf{R}^T(r)\mathbf{S}_a + \mathbf{p}^T(x)\mathbf{S}_b\right]\hat{\mathbf{u}} \tag{33}$$

As seen in eq. (34) and considering definition of a shape function in numerical methods, the shape functions' matrix can be presented as below:

$$\mathbf{\Phi}(x) = \mathbf{R}^T(r)\mathbf{S}_a + \mathbf{p}^T(x)\mathbf{S}_b \tag{34}$$

In the following, the above process is implemented in a 1D 3-node element in the natural coordinate system ξ with arbitrary coordinates in NMM (Fig. 5). The desired complex Fourier RBF can be presented as eq. (35) [38,39]:

$$R(r) = \alpha e^{i\omega r} \tag{35}$$

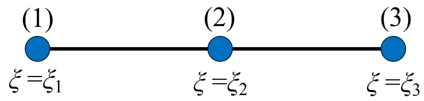

Fig. 5. 1D 3-node element in the natural coordinate system.

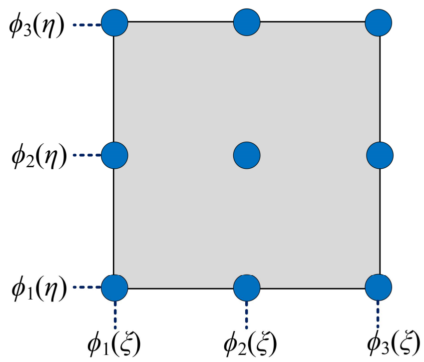

Fig. 6. 2D 9-node complex Fourier element in the natural coordinate system.

in which, α and ω represent shape parameters [40]. For a 1D 3-node natural element, $R(r)$ vector can be written as follows:

$$\mathbf{R}(r) = \begin{bmatrix} R_1(r) \\ R_2(r) \\ R_3(r) \end{bmatrix} = \begin{bmatrix} \alpha e^{i\omega|\xi-\xi_1|} \\ \alpha e^{i\omega|\xi-\xi_2|} \\ \alpha e^{i\omega|\xi-\xi_3|} \end{bmatrix} = \alpha \begin{bmatrix} e^{i\omega|\xi+1|} \\ e^{i\omega|\xi|} \\ e^{i\omega|\xi-1|} \end{bmatrix} \tag{36}$$

It is possible to use constant or linear polynomial fields, for a 3-node element. Equation (37) shows a linear polynomial field.

$$\mathbf{P}(\xi) = \begin{bmatrix} 1 \\ \xi \end{bmatrix} \tag{37}$$

The desired vectors and matrices of the enrichment process of complex Fourier RBFs can be obtained as below [37]:

$$\begin{gathered} \mathbf{R}_Q = \alpha \begin{bmatrix} 1 & e^{i\omega|\xi_1-\xi_2|} & e^{i\omega|\xi_1-\xi_3|} \\ e^{i\omega|\xi_2-\xi_1|} & 1 & e^{i\omega|\xi_2-\xi_3|} \\ e^{i\omega|\xi_3-\xi_1|} & e^{i\omega|\xi_3-\xi_2|} & 1 \end{bmatrix} \rightarrow \mathbf{R}_Q = \alpha \begin{bmatrix} 1 & e^{i\omega} & e^{2i\omega} \\ & 1 & e^{i\omega} \\ \text{Sym.} & & 1 \end{bmatrix}, \\ \mathbf{P}_m = \begin{bmatrix} 1 & \xi_1 \\ 1 & \xi_2 \\ 1 & \xi_3 \end{bmatrix} = \begin{bmatrix} 1 & -1 \\ 1 & 0 \\ 1 & 1 \end{bmatrix} \end{gathered} \tag{38}$$

$$\begin{gathered} \mathbf{S}_a = \frac{1}{2\alpha(1-e^{i\omega})(3-e^{i\omega})} \begin{bmatrix} 1 & -2 & 1 \\ & 4 & -2 \\ \text{Sym.} & & 1 \end{bmatrix}, \\ \mathbf{S}_b = \frac{1}{3-e^{i\omega}} \begin{bmatrix} 1 & 1-e^{i\omega} & 1 \\ -\dfrac{3-e^{i\omega}}{2} & 0 & \dfrac{3-e^{i\omega}}{2} \end{bmatrix} \end{gathered} \tag{39}$$

In the end, the shape functions of a 1D 3-node complex Fourier element can be presented as below:

$$\begin{aligned} &\mathbf{\Phi}(\xi) = [\phi_1(\xi) \quad \phi_2(\xi) \quad \phi_3(\xi)] \\ &\phi_1(\xi) = \frac{1}{2}(-\xi + c + h(\xi)) \\ &\phi_2(\xi) = (1-c) - h(\xi) \\ &\phi_3(\xi) = \frac{1}{2}(\xi + c + h(\xi)) \end{aligned} \tag{40}$$

where $c = \dfrac{2}{3-e^{i\omega}}$ and

$$h(\xi) = \frac{e^{i\omega|\xi+1|} - 2e^{i\omega|\xi|} + e^{i\omega|\xi-1|}}{(1-e^{i\omega})(3-e^{i\omega})} = \frac{e^{i\omega(\xi+1)} - 2e^{i\omega\xi\,\mathrm{sgn}(\xi)} + e^{i\omega(\xi-1)}}{(1-e^{i\omega})(3-e^{i\omega})} \tag{41}$$

As seen in equations, the shape parameter α vanishes and only the shape parameter ω remains.

3.3 2D complex Fourier element

In This section, formulation of a 2D 9-node element is obtained by use of above results. Consider a 2D 9-node complex Fourier element with arbitrary coordinates as shown in Fig. 6. This element's shape functions are accessible by multiplying complex Fourier one-dimensional interpolation functions as shown below:

$$w_{3(r-1)+s}(\xi,\eta)=\phi_r(\xi)\phi_s(\eta) \tag{42}$$

3.4 Properties of complex Fourier shape functions

In this section, the main properties of complex Fourier shape functions that cause them to become more accurate and stable than classic Lagrange shape functions, in the process of approximation, are provided:

3.4.1 Partition of unity

The below relation can be written for an n-node complex Fourier element [18]:

$$\sum_{j=1}^{n} w_j(\boldsymbol{\xi})=1+0i \tag{43}$$

where $\boldsymbol{\xi}=(\xi,\eta)^T$.

3.4.2 Kronecker delta property

The Kronecker delta property of shape functions can be shown as follows:

$$w_m(\boldsymbol{\xi}_n)=\delta_{mn} \tag{44}$$

in which, $\boldsymbol{\xi}_n=(\xi_n,\eta_n)^T$ represents point n and δ_{mn} indicates the Kronecker symbol which is described in eq. (5).

3.4.3 Linear independence property

In general, the basis functions with Kronecker delta property also have the linear independence property, as mentioned in mathematics. The linear independence property of proposed shape functions can be shown as below:

$$\text{If } \sum_{m=1}^{n} c_m w_m(\boldsymbol{\xi};\boldsymbol{\xi}_1,\boldsymbol{\xi}_2,\ldots,\boldsymbol{\xi}_n)=0 \text{ then } c_i=0,\ \ i=1,2,\ldots,n. \tag{45}$$

where $\boldsymbol{\xi}=(\xi,\eta)^T$ and $\boldsymbol{\xi}_i=(\xi_i,\eta_i)^T$. Replacing $\boldsymbol{\xi}$ with $\boldsymbol{\xi}_k(k=1,2,\ldots,n)$ in the above relation and using the Kronecker delta property leads to proving the mentioned property:

$$\left.\begin{array}{c}\displaystyle\sum_{m=1}^{n} c_m w_m(\xi_k)=0 \\ \displaystyle\sum_{m=1}^{n} c_m w_m(\xi_k)=\sum_{m=1}^{n} c_m\delta_{mk}=c_k\end{array}\right\}\rightarrow c_k=0,\quad k=1,2,\ldots,n. \tag{46}$$

3.5 The versatility of complex Fourier shape functions

Both classic Lagrange and complex Fourier shape functions can satisfy polynomial function fields. Moreover, the proposed shape functions also satisfy exponential and trigonometric function fields appeared in additional functions $h(\xi)$.

4. Numerical Examples

In this section, three problems are provided to compare the results of complex Fourier shape functions in NMM with those obtained by classic Lagrange shape functions and, if available, analytical solutions.

4.1 Free vibration of a simple beam

The first example is a simply supported beam with a length of 10 m and height of 0.4 m. At first, the beam is loaded with a constant linear load w= 9.6 KN.m^{-1}. So, by the effect of the load, the beam will statically deflect and becomes fixed. Then, the load is suddenly removed, and the beam dynamically starts to vibrate freely. Figure 7 shows the geometry, loading and boundary conditions. The material properties for this example are E=20000 MN.m^{-2}, ρ=2400 Kg.m^{-3} and ν=0.333.

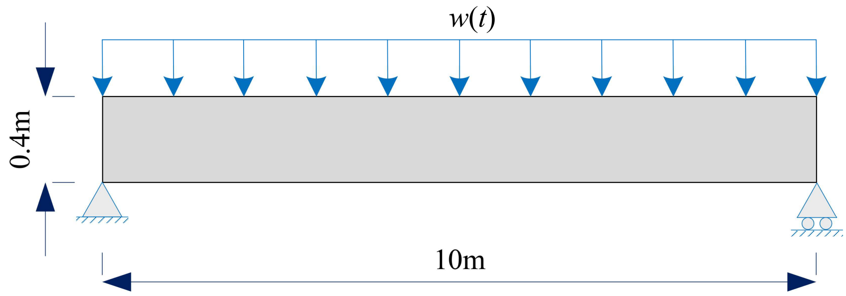

Fig. 7. Geometry, loading and boundary condition of the simply supported beam.

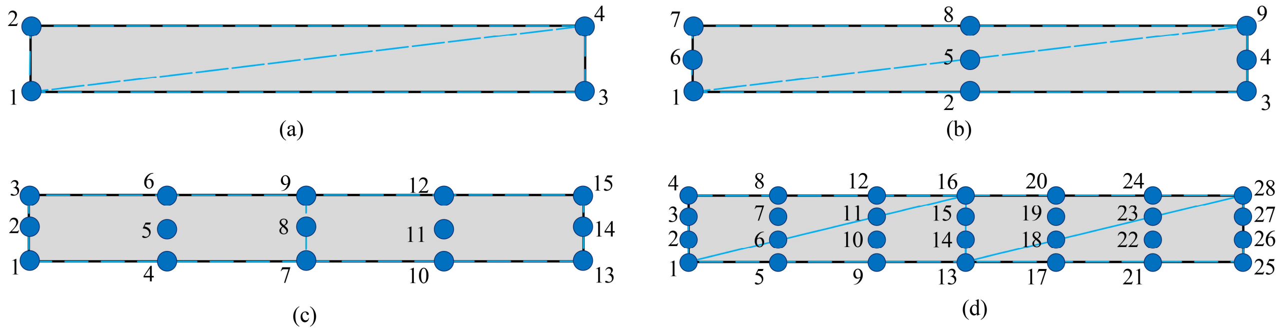

Fig. 8. The Manifold element of the simple beam. (a) Two 3-node triangular elements; (b) Two 6-node triangular elements; (c) Two 9-node quadrilateral element; (d) Four 10-node triangular elements.

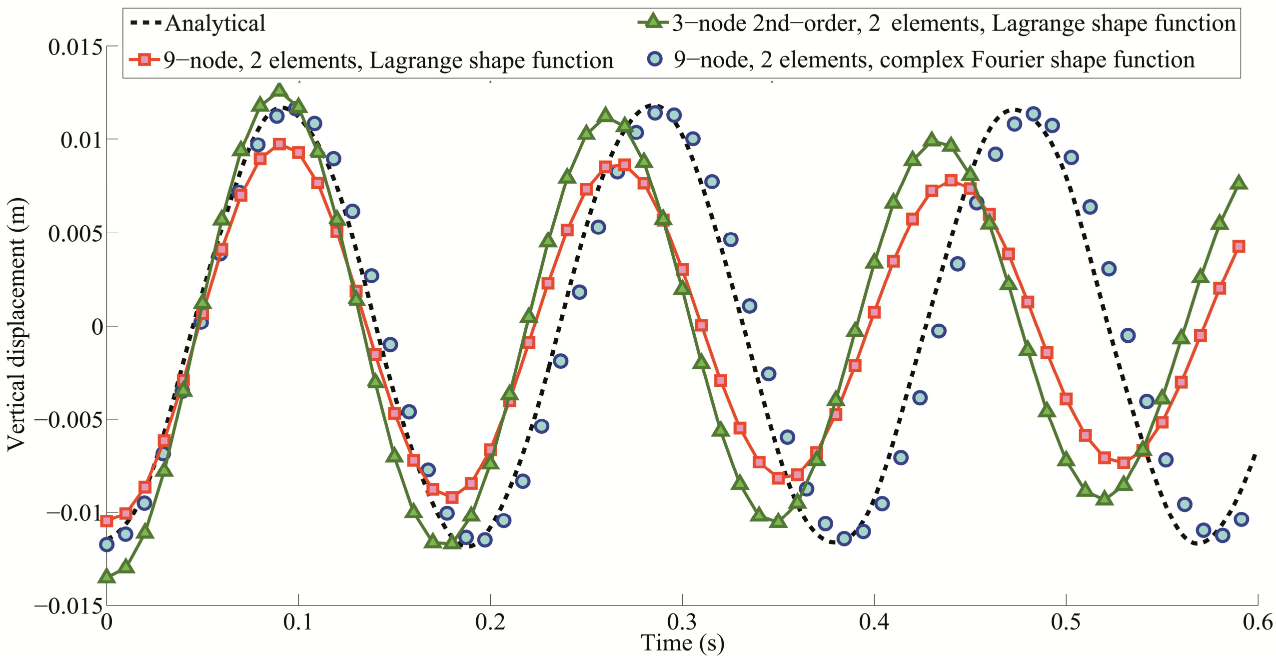

Fig. 9. 9-node NMM with Lagrange shape functions results, proposed complex Fourier shape functions results and analytical results of middle point vibration of the simply supported beam.

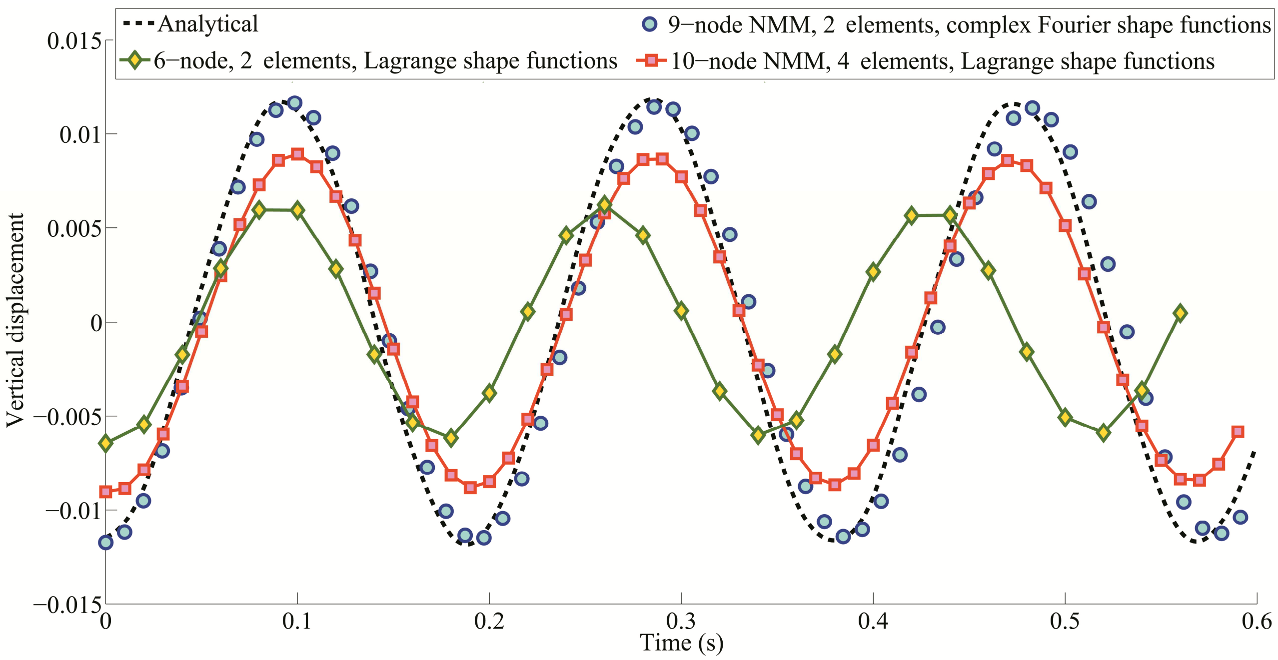

Fig. 10. 9-node, 10-node, 3-node 2nd-order and analytical results of middle point vibration of the simply supported beam.

The midpoint vibration of the beam is used to compare the analytical solutions [41] with the solutions of NMM using approach mentioned above. Figure 8 shows the elements for 3-node, 9-node and 10-node NMM. As shown in Fig. 9, the results of the suggested complex Fourier shape functions are more accurate than Lagrange shape functions in the same manifold order with the same number of elements, and also, they are close to the analytical results. In Fig. 10, 9-node NMM with use of complex Fourier shape functions with the degree of freedom (DOF) of 30 are compared to 10-node triangular (DOF=56) and 6-node triangular with Lagrange shape functions and 2nd-order NMM with Lagrange shape functions (Fig.8) and as the figure shows, 9-node NMM with complex Fourier shape functions is more accurate than the other methods, even with lower DOF.

4.2 Deep beam with simple supports under Heaviside step function loading

Suppose that a deep beam with the height of 6 and width of 24 is simply supported at both ends. The geometry, loading and boundary conditions are shown in Fig. 11(a). The deep beam is subjected to a uniformly distributed Heaviside step function loading $w(t)=0.01H(t-0)$ (Fig. 11(b)). Other properties for this example are $E=100$, $\rho=1.5$ and $\nu=0.333$. Since symmetry condition is applicable, half of the beam is modeled (see Fig. 11(c)).

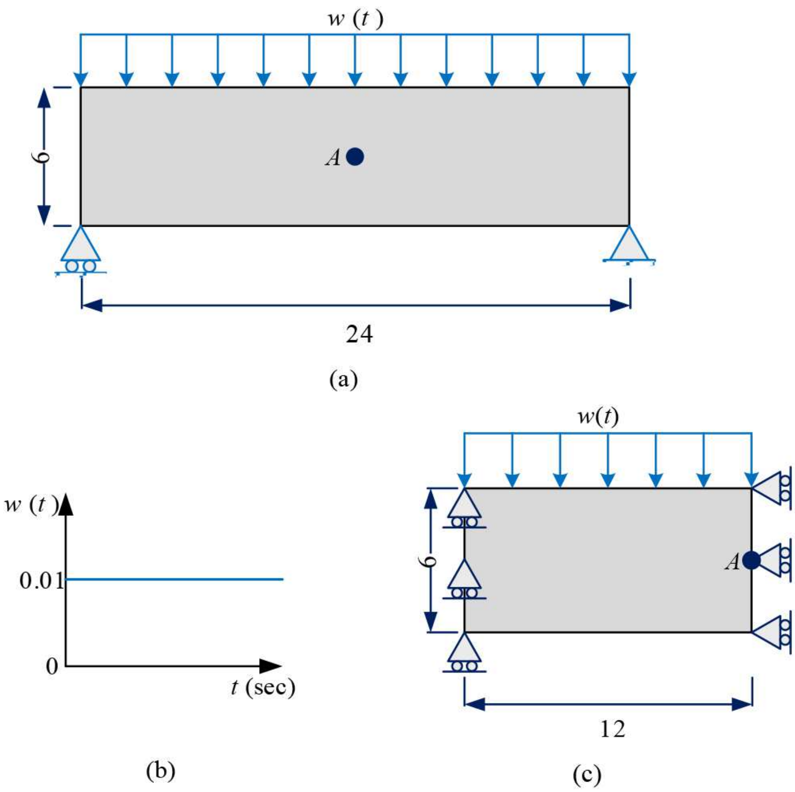

Fig. 11. Deep beam with simple supports under $w(t)=0.01H(t-0)$ load. (a) Geometry and boundary conditions of the beam; (b) Loading; (c) Half of the beam.

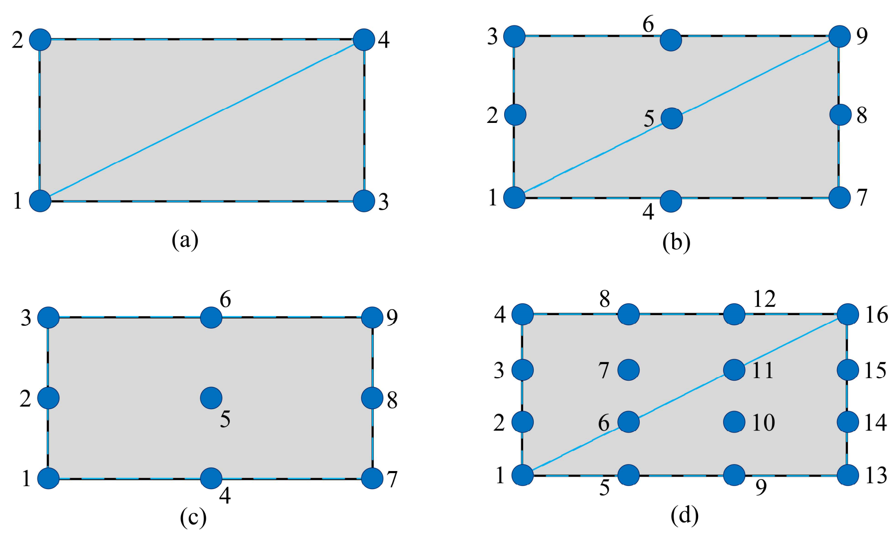

Fig. 12. Manifold elements of the deep beam. (a) Two 3-node elements; (b) two 6-node elements; (c) one 9-node element (d) two 10-node element.

Figure 12 shows the elements for 9-node, 6-node, 10-node and conventional 3-node element NMM. Figure 13 shows the vertical displacement time history of point A, which is used to compare the results of 9-node NMM using suggested shape functions with 9-node NMM and 3-node NMM with classic Lagrange ones and the results of Samaan and Rashed [42]. As seen in the figure, results of both 9-node NMMs, which use 18 degrees of freedom, are more accurate than 2nd-order 3-node NMM that uses 24 degrees of freedom. Furthermore, the results of complex Fourier shape functions are more accurate than Lagrange shape functions in the same manifold order and the same number of elements. The results for 6-node NMM, 10-node NMM and 3-node 3rd-order NMM with Lagrange shape functions are shown in Fig. 14. Comparing Fig. 13 and Fig. 14, 9-node NMM with complex Fourier shape functions (DOF=18) is more accurate than 3rd-order NMM (DOF=40). Also, the results of suggested shape functions with lower degrees of freedom almost match the ones of Samaan and Rashed [42] (DOF=96).

4.3 Infinite rectangular strip under Heaviside step function loading

An infinite strip with a rectangular cross-section which has a height of 4 m and width of 2 m is enclosed from three sides with roller supports. The upper edge is uniformly subjected to a Heaviside step function $P(t)=H(t-0)$ (Fig. 15). The material properties are as follows: E=0.1 MN.m^{-2}, ρ=1 Kg.m^{-3} and ν=0.25.

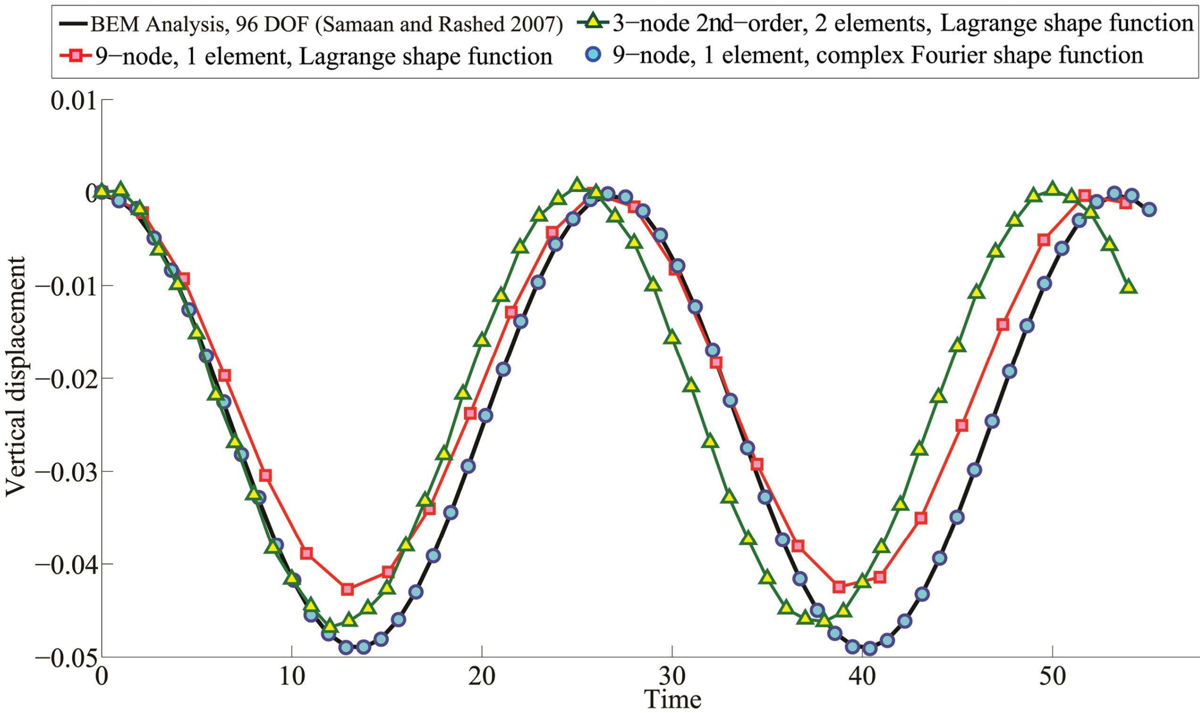

Fig. 13. 9-node with Lagrange and proposed complex Fourier shape functions, 3-node 2nd-order and analytical results of middle point vibration of the deep beam.

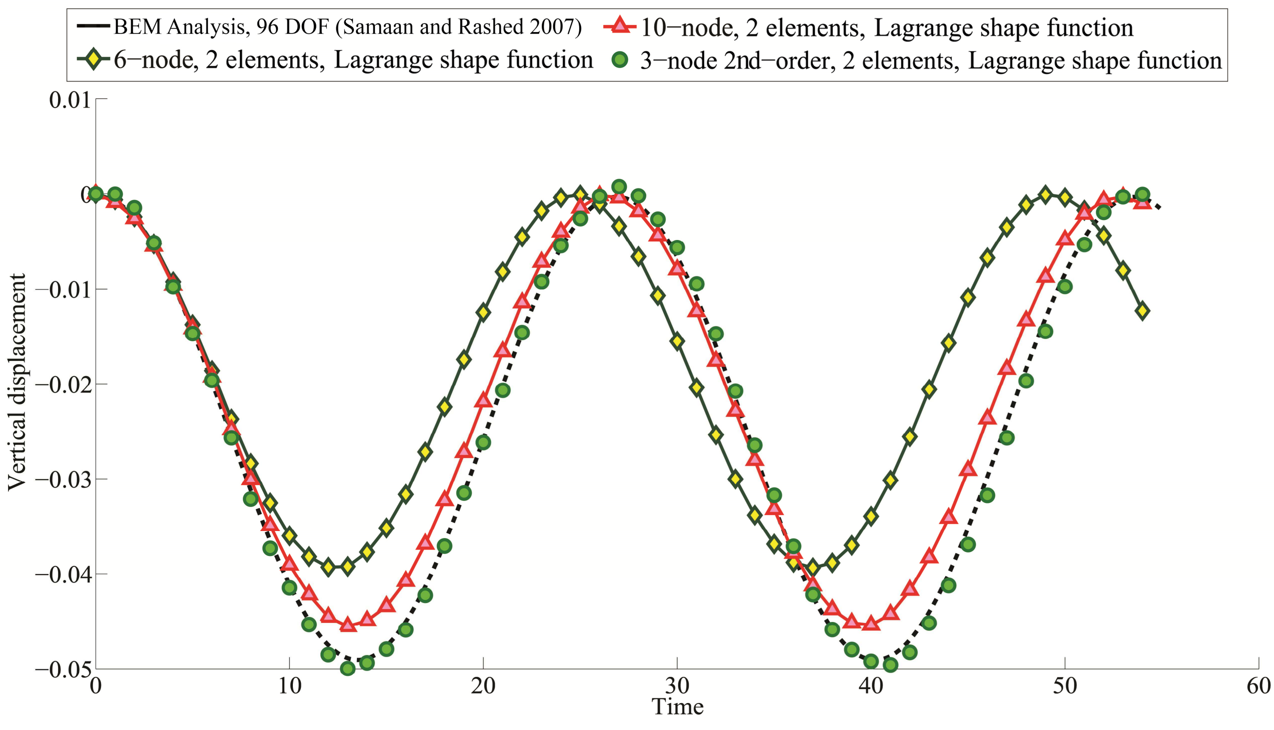

Fig. 14. 6-node, 10-node, 3-node 3rd-order and analytical results of middle point vibration of the deep beam.

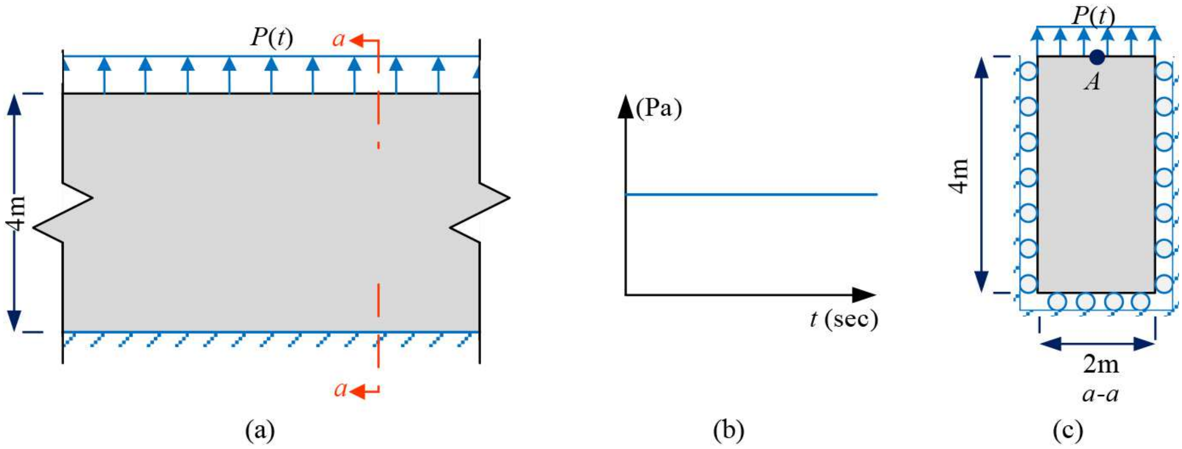

Fig. 15. Infinite rectangular strip under load $P(t)=H(t-0)$. (a) Geometry and boundary conditions; (b) Loading; (c) Section a-a.

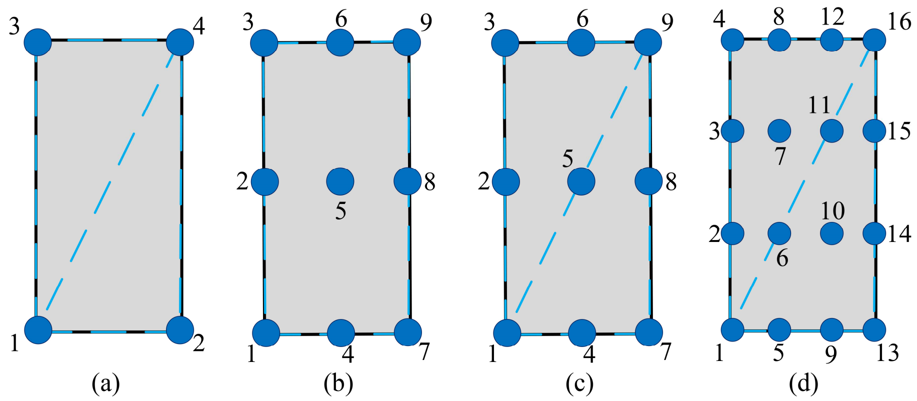

Fig. 16. Manifold elements of the infinite rectangular strip. (a) Two 3-node elements; (b) one 9-node element; (c) Two 6-node elements; (d) Two 10-node elements.

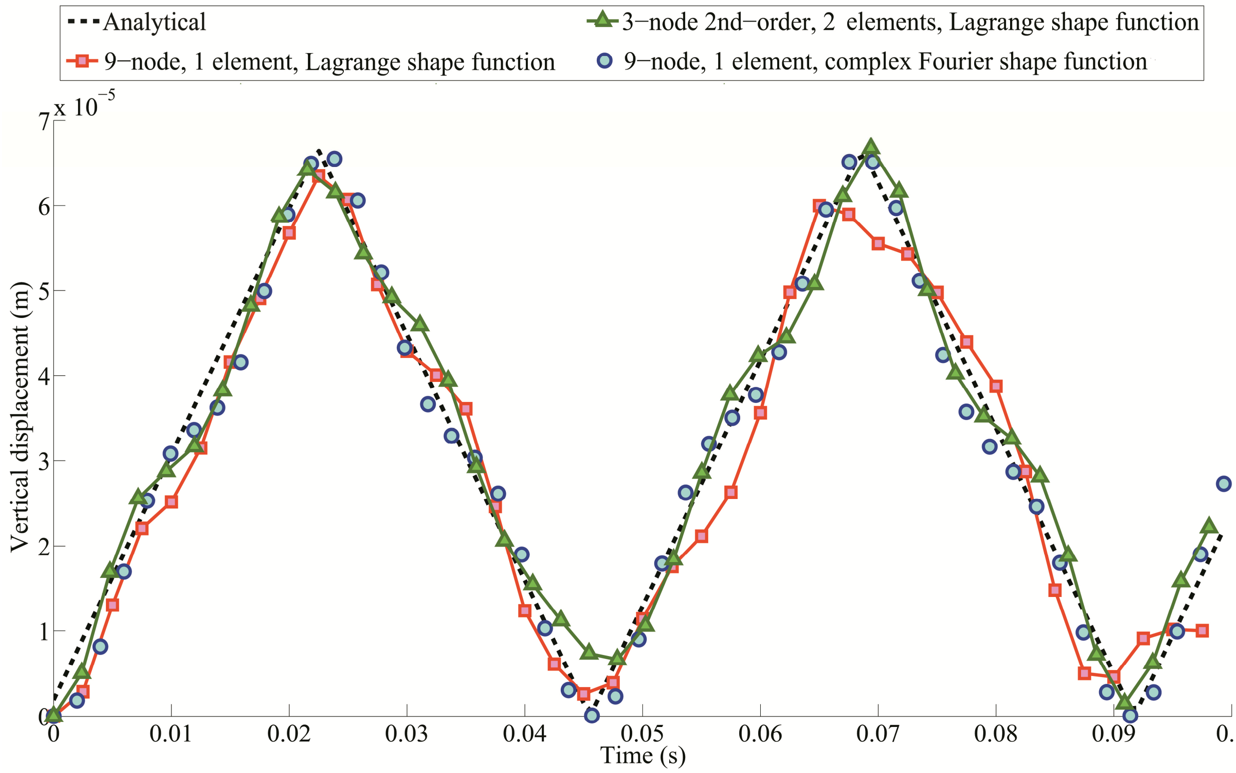

Fig. 17. 9-node NMM with Lagrange shape functions results, proposed shape functions results, 3-node 2nd-order and analytical results of point A vibration.

As shown in Fig. 16, to mesh the problem, one 9-node element, two 3-node elements, two 6-node elements and two 10-node elements are used. The displacement time history of point A for 9-node and 2nd-order 3-node triangular NMM with complex Fourier shape functions and 9-node Lagrange shape functions and the analytical results [43] are indicated in Fig. 17. As seen in the figure, 9-node NMM with proposed shape functions (DOF=18) results are more accurate than 2nd-order 3-node NMM with the complex Fourier shape functions results (DOF=24) [44], and also more accurate than 9-node NMM Lagrange shape functions in the same manifold order and with the same number of elements. Also, in Fig.18 results of 9-node NMM with proposed shape functions are compared to 6-node (DOF=18) and 10-node (DOF=32) triangle NMM with Lagrange shape functions, and it can be seen that 9-node NMM with proposed shape functions is more accurate than other methods.

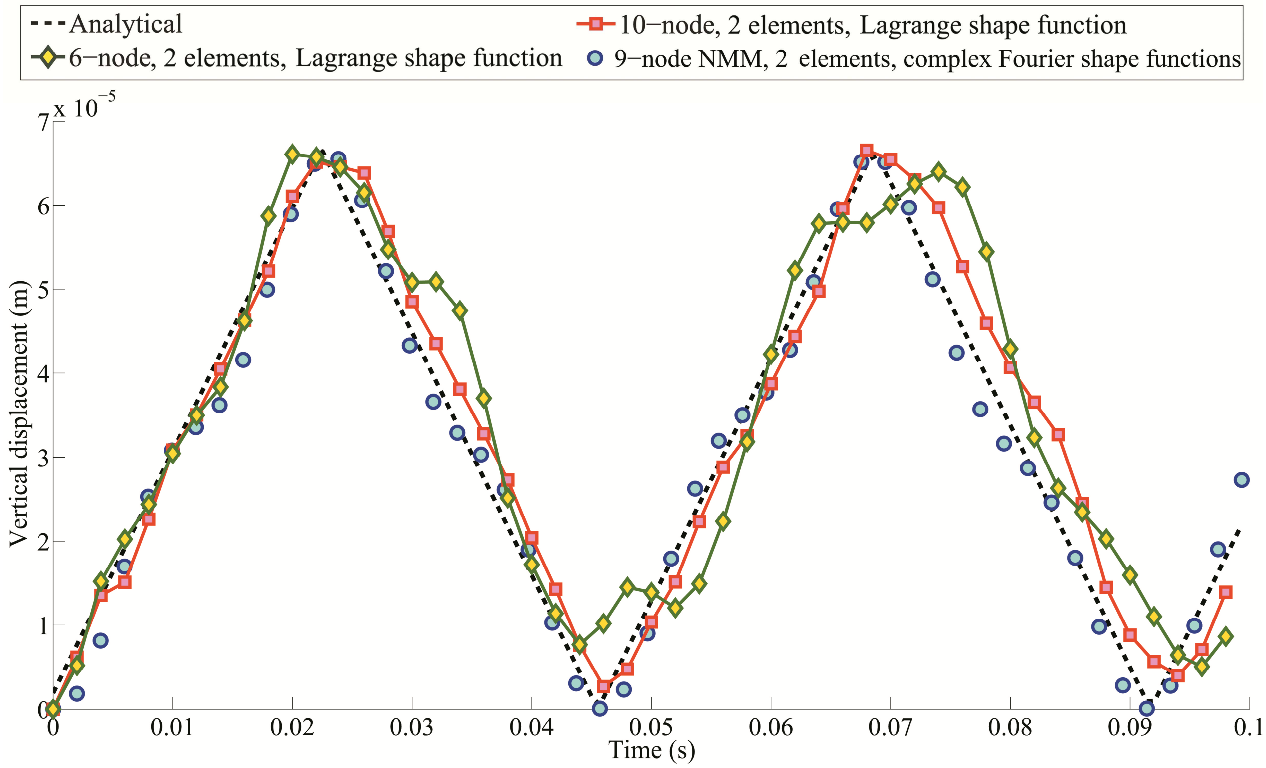

Fig. 18. 6-node, 10-node NMM with Lagrange shape functions, 9-node NMM with complex Fourier shape functions and analytical results of point A vibration.

5. Conclusions

In this paper, the new 9-node quadrilateral and 10-node triangular elements were proposed, and also, in addition to Lagrange shape functions, complex Fourier shape functions were used to improve the results of 9-node quadrilateral NMM. The most remarkable advantage of these proposed shape functions over classic Lagrange ones is satisfying polynomial, trigonometric and exponential function fields simultaneously. Also these shape functions have some useful properties which the most important of them in NMM is linear independence property. As mentioned, construction of high-order NMM is applicable in two ways; the first way is increasing the order of weight functions which increases the number of nodes of each element and thus remeshing the desirable domain is needed for the increase of each degree. The second way is increasing the order of local approximation functions which is simpler compared to the first approach, but the probability of linear dependence occurring is an obstacle in this approach. Some numerical examples were provided to challenge the proposed methods in free vibration and also forced vibration. These examples showed high accuracy of the proposed 9-node quadrilateral element and 10-node triangular element compared with 3-node and 6-node triangular NMM, and also the superiority of complex Fourier shape functions over conventional Lagrange shape functions.

Author Contributions

Complex Fourier RBFs and subject definition were planned by the second and third authors and in advancing the scheme, the first author utilized the proposed RBFs in NMM. The first author wrote the initial manuscript and then it was technically edited by the second and third authors. The manuscript was written through the contribution of all authors. All authors discussed the results, reviewed, and approved the final version of the manuscript.

Conflict of Interest

The authors declared no potential conflicts of interest with respect to the research, authorship, and publication of this article.

Funding

The authors received no financial support for the research, authorship, and publication of this article.

Nomenclature

u	Displacement [m]	ρ	Density [Kg/m^3]
$\ddot{u}$	Acceleration [m/s^2]	ν	Poisson's ration
E	Young's modulus [Pa]		

References

[1] Shi, G., Manifold Method of Material Analysis, *Transactions of the Ninth Army Conference on Applied Mathematics and Computing*, Minneapolis, MN, US, 1992.

[2] Shi, G., Modeling Rock Joints and Blocks by Manifold Method, *Rock Mechanics Proceedings of the 33rd US Symposium*, Santa Fe, NM, US, 1992.

[3] Chen, G., A View on Manifold Method Comparing with Finite Element Method. *In: Computational Mechanics*, Heidelberg, Germany, 2007.

[4] Li, S., Cheng, Y., Wu, Y.F., Numerical Manifold Method Based on the Method of Weighted Residuals, *Computational Mechanics*, 35(6), 2005, 470-480.

[5] Oden, J.T., Duarte, C.A.M., Zienkiewicz, O.C., A New Cloud-based hp Finite Element Method, *Computer Methods in Applied Mechanics and Engineering*, 153(1-2), 1998, 117-126.

[6] Ghasemzadeh, H., Ramezanpour, M.A., Bodaghpour, S., Dynamic High Order Numerical Manifold Method Based on Weighted Residual Method, *International Journal for Numerical Methods in Engineering*, 100(8), 2014, 596-619.

[7] Fan, H., Zheng, H., He, S., Jiang, Z., A novel numerical manifold method with derivative degrees of freedom and without linear dependence, *Engineering Analysis with Boundary Elements*, 64, 2016, 19-37.

[8] Zheng, H., Xu, D., New Strategies for Some Issues of Numerical Manifold Method in Simulation of Crack Propagation, *International Journal for Numerical Methods in Engineering*, 97(13), 2014, 986-1010.

[9] Chen, Y.L., Li, L.X., An improved numerical manifold method and its application, *Engineering Analysis with Boundary Elements*, 52, 2015, 120-129.

[10] Chern, J.C., Koo, C.Y., Chen, S., Development of Second Order Displacement Function for DDA and Manifold Method, *In: Working Forum on the Manifold Method of Material Analysis*, Vicksburg, Mississippi, United States, Vol.1, p.183, 1997.

[11] Fouda, N., El-Midany, T., Sadoun, A.M., Bending, Buckling and Vibration of a Functionally Graded Porous Beam Using Finite Elements, *Journal of Applied and Computational Mechanics*, 3(4), 2017, 274-282.

[12] Darwich, A., Nazha, H., Daoud, M., Effect of Coating Materials on the Fatigue Behavior of Hip Implants: A Three-dimensional Finite Element Analysis, *Journal of Applied and Computational Mechanics*, 6(2), 2020, 284-295.

[13] Manconi, E., Sorokin, S., Garziera, R., Soe-Knudsen, A., Wave Motion and Stop-bands in Pipes with Helical Characteristics Using Wave Finite Element Analysis, *Journal of Applied and Computational Mechanics*, 4, 2018, 420-428.

[14] Surendran, M., Pramod, A.L.N., Natarajan, S., Evaluation of Fracture Parameters by Coupling the Edge-based Smoothed Finite Element Method and the Scaled Boundary Finite Element Method, *Journal of Applied and Computational Mechanics*, 5, 2019, 540-551.

[15] Shyu, K., Salami, M.R., Manifold Method with Four-node Isoparametric Finite Element Mesh, *In: Working Forum on the Manifold Method of Material Analysis*, Vicksburg, Mississippi, United States, Vol.1, p.165, 1997.

[16] Zhang, G.X., Sugiura, Y., Hasegawa, H., Wang, G., The Second Order Manifold Method with Six Node Triangle Mesh, *Structural Engineering/Earthquake Engineering*, 19(1), 2002, 1s-9s.

[17] Fan, H., He, S., Jiang, Z., A High-order Numerical Manifold Method with Nine-node Triangular Meshes, *Engineering Analysis with Boundary Elements*, 61, 2015, 172-182.

[18] Hamzehei-Javaran, S., Khaji, N., Moharrami, H., A Dual Reciprocity BEM Approach Using New Fourier Radial Basis Functions Applied to 2D Elastodynamic Transient Analysis, *Engineering Analysis with Boundary Elements*, 35(1), 2011, 85-95.

[19] Hamzehei-Javaran, S., Khaji, N., Noorzad, A., First Kind Bessel Function (J-Bessel) as Radial Basis Function for Plane Dynamic Analysis Using Dual Reciprocity Boundary Element Method, *Acta Mechanica*, 218(3-4), 2011, 247-258.

[20] Izadpanah, E., Shojaee, S., Hamzehei-Javaran, S., A Time-dependent Discontinuous Galerkin Finite Element Approach in Two-dimensional Elastodynamic Problems Based on Spherical Hankel Element Framework, *Acta Mechanica*, 229(12), 2018, 4977–4994.

[21] Bahrampour, M., Hamzehei-Javaran, S., Shojaee, S., New Insight into Viscoelastic Finite Element Modeling of Time-dependent Material Creep Problems Using Spherical Hankel Element Framework, *International Journal of Applied Mechanics*, 10(8), 2018, 1850085.

[22] Hamzehei-Javaran, S., Shojaee, S., Improvement of Numerical Modeling in the Solution of Static and Transient Dynamic Problems Using Finite Element Method Based on Spherical Hankel Shape Functions, *International Journal for Numerical Methods in Engineering*, 115, 2018, 1241–1265.

[23] Mohebbi, A., Saffarian, M., Implicit RBF Meshless Method for the Solution of Two-dimensional Variable Order Fractional Cable Equation, *Journal of Applied and Computational Mechanics*, 6(2), 2020, 235-247.

[24] Hamzehei-Javaran, S., Shojaee, S., The Solution of Elastostatic and Dynamic Problems Using the Boundary Element Method Based on Spherical Hankel Element Framework, *International Journal for Numerical Methods in Engineering*, 112, 2017, 2067–2086.

[25] Izadpanah, E., Shojaee, S., Hamzehei-Javaran, S., Time Discontinuous Finite Element Analysis of Two-dimensional Elastodynamic Problems Using Complex Fourier Shape Functions, *Journal of Applied and Computational Mechanics*, 5, 2018, 442-456.

[26] Farmani, S., Ghaeini-Hessaroeyeh, M., Hamzehei-Javaran, S., The Improvement of Numerical Modeling in the Solution of Incompressible Viscous Flow Problems Using Finite Element Method Based on Spherical Hankel Shape Functions, *International Journal for Numerical Methods in Fluids*, 87(2), 2018, 70-89.

[27] Bahrampour, M., Hamzehei-Javaran, S., Shojaee, S., Spherical Hankel-based Creep Analysis of Time Dependent Materials Using Boundary Element Theories, *Journal of Engineering Mechanics ASCE*, 146(6), 2020, 04020050.

[28] Mohammadi Nia, M., Shojaee, S., Hamzehei-Javaran, S., Utilizing New Spherical Hankel Shape Functions to Reformulate the Deflection, Free Vibration, and Buckling Analysis of Mindlin Plates Based on Finite Element Method, *Scientia Iranica*, 2018, https://doi.org/10.24200/sci.2018.5113.1103.

[29] Farmani, S., Ghaeini-Hessaroeyeh, M., Hamzehei-Javaran, S., Development of a New Numerical Model for Sloshing Behavior in 2-D Tanks Based on Nonlinear Finite Element Method, *Journal of Engineering Mechanics (ASCE)*, 145(12), 2019, 04019107.

[30] Attaran, B., Ghanbarzadeh, A., Bearing Fault Detection Based on Maximum Likelihood Estimation and Optimized ANN Using the Bees Algorithm, *Journal of Applied and Computational Mechanics*, 1(1), 2014, 35-43.

[31] Farmani, S., Ghaeini-Hessaroeyeh, M., Hamzehei-Javaran, S., Increasing the Solution Accuracy in the Numerical Modeling of Boundary Value Problems Using Finite Element Method Based on Hankel Shape Functions, *International Journal of Applied Mechanics*, 2019, DOI: 10.1142/S1758825119500625.

[32] Mohammadi Nia, M., Shojaee, S., Hamzehei-Javaran, S., A Mixed Formulation of B-spline and a New Class of Spherical Hankel Shape Functions for Modeling Elastostatic Problems, *Applied Mathematical Modelling*, 77, 2020, 602-616.

[33] Chen, G., Ohnishi, Y., Ito, T., Development of High-order Manifold Method, *International Journal for Numerical Methods in Engineering*, 43(4), 1998, 685–712.

[34] Irons, B.M., Engineering Applications of Numerical Integration in Stifness Methods, *Journal of the American Institute of Aeronautics and Astronautics*, 4(11), 1966, 2035– 2037.

[35] Zienkiewicz, O.C., Taylor, RL., *The Finite Element Method Vol.1 4th.edn*, McGraw-hill, Butterworth, London, UK, 2000.

[36] Khaji, N., Hamzehei-Javaran, S., New Complex Fourier Shape Functions for the Analysis of Two-dimensional Potential Problems Using Boundary Element Method, *Engineering Analysis with Boundary Elements*, 37(2), 2013, 260-272.

[37] Hamzehei-Javaran, S., Approximation of the State Variables of Navier's Differential Equation in Transient Dynamic Problems Using Finite Element Method Based on Complex Fourier Shape Functions, *Asian Journal of Civil Engineering*, 19, 2018, 431-450.

[38] Hamzehei-Javaran, S., Khaji, N., Dynamic Analysis of Plane Elasticity with New Complex Fourier Radial Basis Functions in the Dual Reciprocity Boundary Element Method, *Applied Mathematical Modelling*, 38(14), 2014, 3641-3651.

[39] Hamzehei-Javaran, S., Khaji, N., Complex Fourier Element Shape Functions for Analysis of 2D Static and Transient Dynamic Problems Using Dual Reciprocity Boundary Element Method, *Engineering Analysis with Boundary Elements*, 95, 2018, 222-237.

[40] Wang, J.G., Liu, G.R., On the Optimal Shape Parameters of Radial Basis Functions Used for 2-D Meshless Methods, *Computer Methods in Applied*

Mechanics and Engineering, 191(2324), 2002, 2611-2630.
[41] Rao, S.S., *Vibration of Continuous Systems*, John Wiley & Sons, New Jersey, US, 2007.
[42] Samaan, M.F., Rashed, Y.F., BEM for Transient 2D Elastodynamics Using Multiquadric Functions, *International Journal of Solids and Structures*, 44(25-26), 2007, 8517-8531.
[43] Dominguez, J., *Boundary Eements in Dynamics*, Wit Press, New Forest, UK, 1993.
[44] Malekzadeh, M., Hamzehei-Javaran, S., Shojaee, S., Novel Insight into High-Order Numerical Manifold Method Using Complex Fourier Element Shape Functions in Statics and Dynamics, *International Journal of Applied Mechanics*, 11(6), 2019, 1950058.

ORCID iD

Mohammad Malekzadeh https://orcid.org/0000-0001-5901-0869
Saleh Hamzehei-Javaran https://orcid.org/0000-0002-7341-4314
Saeed Shojaee https://orcid.org/0000-0003-0952-9085

How to cite this article: Malekzadeh M., Hamzehei-Javaran S., Shojaei S. Improvement of Numerical Manifold Method using Nine-node Quadrilateral and Ten-node Triangular Elements along with Complex Fourier RBFS in Modeling Free and Forced Vibrations, *J. Appl. Comput. Mech.*, 7(4), 2021, 2049–2063. https://doi.org/10.22055/JACM.2020.32423.2027